



1 **Thrusts control the thermal maturity of accreted sediments**

2 Utsav Mannu^{1,*}, David Fernández-Blanco², Ayumu Miyakawa³, Taras Gerya⁴, and Masataka Kinoshita⁵

3 ¹Discipline of Earth Sciences, Indian Institute of Technology, Gandhinagar, India

4 ²Barcelona Center of Subsurface Imaging, Institut de Ciències del Mar (ICM-CSIC), Barcelona, Spain;

5 ³Geological Survey of Japan, AIST

6 ⁴Institute of Geophysics, ETH Zurich

7 ⁵Earthquake Research Institute, UTokyo

8 *Correspondence to:* Utsav Mannu (utsav.mannu@iitgn.ac.in)

9

10

11

12

13

14

15

16

17

18

19



20 **Abstract.**

21 Thermal maturity assessments of hydrocarbon-generation potential and thermal history rarely consider how upper-plate
22 structures developing during subduction influence the trajectories of accreted sediments. Our thermomechanical models of
23 subduction support that thrusts evolving under variable sedimentation rates and décollement strengths fundamentally influence
24 the trajectory, temperature, and thermal maturity of accreting sediments. This is notably true for the frontal thrust, which
25 pervasively partitions sediments along a low and a high maturity path. Our findings imply that interpretations of the distribution
26 of thermal maturity cannot be detached from accounts of the length and frequency of thrusts and their controlling factors.
27 Taking these factors into consideration, our approach provides a robust uncertainty estimate in maximum exposure
28 temperatures as a function of vitrinite reflectance and burial depth thereby reducing former inconsistencies between predicted
29 and factual thermal maturity distributions in accretionary wedges.

30
31
32
33
34
35
36
37
38
39
40
41
42
43
44
45
46
47
48
49
50



51 1. Introduction

52 Organic material transforms into coal, oil, and gas at rates primarily controlled by temperature (Quigley & Mackenzie, 1988).
53 This transformation, critical for the hydrocarbon industry, is also useful to study the tectonic and sedimentary evolution of
54 basins and orogens (Tissot et al., 1987; Tissot & Welte, 2013; Waples, 1981). The extent of this transformation in sediments,
55 known as thermal maturity, can be measured as vitrinite reflectance; the percentage of incident light reflected from the surface
56 of vitrinite particles in those sediments (Burnham & Sweeney, 1989). Thermal maturity has been used to estimate the thermal
57 evolution of igneous intrusions (Bostick & Pawlewicz, 1984) and seismic slip (Rabinowitz et al., 2020), the extent of diagenesis
58 and low-grade metamorphism (Ferreiro Mählmann & Le Bayon, 2016; Totten & Blatt, 1993), porosity and compaction in basin
59 sediments (Schmoker & Gautier, 1988), as well as the geothermal history of accreting material during subduction (A.
60 Sakaguchi et al., 2011; Underwood et al., 1992; Yamamoto et al., 2017).

61 Inferences on the geothermal history of subduction margins based on thermal maturity depend on the trajectory
62 followed by the accreting sediments (Miyakawa et al., 2019). Low-temperature high-pressure metamorphic rocks in the
63 subduction wedge are often attributed to the pressure maxima that typically predate the temperature maxima in sediments
64 accreted in the wedge (Platt, 1993). However, numerical models (Ruh, 2020b) and field observations (Giunchi & Ricard, 1999)
65 have indicated the existence of complicated patterns in sediment trajectories. As the orogenic wedge evolves, sediments
66 accreting along different paths reach different depths and velocities and are exposed to different regional peak temperatures.
67 Miyakawa (2019) proposed to subdivide these trajectories based on their final characteristics such as thermal maturity. As a
68 result, the spatiotemporal evolution of the sediments which regulate thermal maturity is controlled, to a first-order, by the
69 partition of incoming sediments along two end-member pathways; (i) a deeper path leading to elevated thermal maturities, the
70 ***high thermal-maturity path***, and (ii) a shallower path resulting in low thermal maturity, the ***low thermal-maturity path***
71 (Miyakawa et al., 2019).

72 Although a number of researchers have studied the diversity of particle paths by their Pressure-Temperature evolution
73 in accreted and underthrust sediments, in presence of surface processes, distribution of surface processes, in both analytical
74 and numerical models (Hori & Sakaguchi, 2011; Elena Konstantinovskaia & Malavieille, 2005; Platt, 1986; Ruh, 2020a; Wenk
75 & Huhn, 2013), its correlation or lack thereof with its pre-accreted state has not been suitably investigated. Much remains to



76 be explored regarding how the partition of high/low thermal maturity paths and the general translation of sediments occurs
77 inside the wedge, given the conventional assumption that accreting sediments remain at the same relative depth (Hori &
78 Sakaguchi, 2011) and translate along the adjacent “layers” without vertical mixing throughout the tectonic evolution of the
79 wedge (Luján et al., 2010; S. Willett et al., 1993) to yield this diversity of sediment paths. To better understand the time-depth
80 paths of wedge sediments, their dependence on the initial state of undeformed sediments, and thus their thermal maturity, the
81 factors that control the evolution of subduction-accretion systems, like sedimentation, erosion, and décollement strength
82 (Mannu et al., 2016; Simpson, 2010), ought to be considered.

83 Here, we explore in detail the impact that a realistic account of accretion in a subduction wedge has on the thermal
84 maturity of its sediments. We simulate subduction-accretion using 2D finite-difference thermomechanical models
85 incorporating empirical thermal conductivity values from the Nankai accretionary margin. We track the evolution of thermal
86 maturity by computing vitrinite reflectance(%R₀) using three well-established methods of %R₀ computation, on each marker
87 in the model as the wedge develops by accretion under different sedimentation rates and décollement strengths. These factors
88 notably alter the trajectories and thermal maturities of incoming sediments. Particularly, thrusts define sharp thermal maturity
89 boundaries leading to stark differences in the thermal maturity of sediments that accrete in different thrust blocks, even when
90 they follow similar trajectories and lay nearby.

91

92 **2. Methods**

93 We employ I2VIS, a conservative (Gerya, 2019) finite-difference 2-D thermomechanical subduction-accretion model with
94 visco-plastic/brittle rheology (Gerya & Yuen, 2003). The code solves the governing equations for the conservation of mass,
95 momentum, and heat as well as the advection equation with a non-diffusive marker-in-cell scheme (Gerya, 2019) constrained
96 by thermal conductivity values inferred from Nankai accretionary wedge (Sugihara et al., 2014). Our numerical approach has
97 several advantages over earlier models to simulate thermal maturity in an accretionary wedge (Miyakawa et al., 2019), such as
98 a more realistic geothermal profile, variable particle paths, and thermal evolution. The supplementary material contains
99 information regarding the governing equations, the modified thermal conductivity formulations based on the C0002 borehole



100 in the Nankai accretionary wedge, boundary conditions, the rheological model, model setup (Fig S1) and surface processes (Fig
101 S2).

102 ***2.1 An improved thermal maturity calculation***

103 Given that assessments of thermal maturity are inherently reliant on the distribution of temperature inside the wedge, any
104 attempt to model thermal maturity needs a realistic temperature gradient in the wedge. We incorporate this by modifying the
105 thermal conductivity computation for sediments and décollement (see Table 1 and section 1 in the provided supplementary
106 text) to match the empirical relationship between depth and thermal conductivity, as measured on core samples in the borehole
107 IODP Site C0002 (Sugihara et al., 2014; Tobin et al., 2015). Both for the same accretionary wedge is scarce to find, and to our
108 knowledge, the C0002 borehole in Nankai accretionary wedge along the Kumano forearc basin is the only place with available
109 datasets for both thermal conductivity and thermal maturity values for an accretionary wedge (Fukuchi et al., 2017). The model
110 computes the $\%R_0$ of each marker to estimate the thermal maturity of sediments during the model run using three widely used
111 methods of thermal maturity modelling Easy $\%R_0$ (Burnham & Sweeney, 1989), Simple $\%R_0$ (Suzuki et al., 1993) and Basin $\%R_0$
112 (Nielsen et al., 2017). All these approaches for computing $\%R_0$ yield similar trends albeit different absolute values. In the
113 interest of clarity, we have mostly illustrated Easy $\%R_0$, which is the most extensively used method for Vitrinite Reflectance
114 computation. Hence, in the interest of clarity, we have mostly illustrated Easy $\%R_0$, which is the most extensively used method
115 of Vitrinite Reflectance computation. Hence, hereafter we refer Easy $\%R_0$ as simply $\%R_0$, unless explicitly stated. $\%R_0$ is set
116 to 0.2 in sediment markers at the start of the model till 2.5 Myr, while $\%R_0$ in markers for other rocks, air, and water is
117 undefined at all times. After 2.5 Myr, the model computes $\%R_0$ on each marker as a function of temperature (T), time (t), and
118 amount of fixed carbon as a percentage (f_c). The initial $\%R_0$ of newly deposited sediments is computed using an assumed
119 water-sediment interaction temperature assumed to be the same as the thermocline. The thermocline used in the model has
120 been estimated using the data obtained and made freely available by International Argo Program and the national programs
121 that contribute to it for the region near Nankai (Argo, 2022). $\%R_0$ is set to 0.2 in sediment markers at the start of the model till 2.5
122 Myr, while $\%R_0$ in markers for other rocks, air, and water is undefined at all times. After 2.5 Myr, the model computes $\%R_0$
123 on each marker as a function of temperature (T), time (t), and amount of fixed carbon as a percentage (f_c). The initial $\%R_0$ of
124 newly deposited sediments is computed using a water-sediment interaction temperature assumed to be the same as the



125 thermocline. The thermocline used in the model has been estimated using the data obtained and made freely available by
126 International Argo Program and the national programs that contribute to it for the region near Nankai (Fig S3, Argo, 2022).

127 **2.2 Experimental Strategy**

128 Here, we present a total of 10 models that vary in their effective basal friction or their effective sedimentation rate to discern
129 patterns of thermal maturity evolution in wedge sediments. Models $M_0^2, M_0^7, M_0^{12}, M_0^{17}, M_0^{22}$, have no sedimentation and
130 effective internal angle values for the décollement of $\phi_b = 2^\circ, 7^\circ, 12^\circ, 17^\circ$ and 22° respectively. The chosen range of effective
131 décollement strength is well within the range of values postulated by several studies for the Nankai accretionary wedge (Tesei
132 et al., 2015). The rest of the models shown here, $M_{0.1}^{12}, M_{0.3}^{12}, M_{0.5}^{12}, M_{0.7}^{12}$, and $M_{0.9}^{12}$ have a medium-strength décollement and
133 variable effective sedimentation rate ranging from 0.1 to 0.9 mm/yr. Sedimentation occurs only at the trench in all of the
134 models presented in this study from sea to land. With these models, we evaluate the particle trajectory and %R₀ of accreting
135 sediments as a function of décollement strength ($M_{0.1}^{12} - M_{0.9}^{12}$) and sedimentation rate ($M_{0.1}^{12} - M_{0.9}^{12}$). To restrict the number of
136 parameters influencing our observations, models have no erosion. Moreover, all models lack surface processes during the
137 first ~2.5 Myr and have sedimentation thereafter. Sediments used in the model have an angle of friction of 30° and a strain-
138 softened value of 20° after a threshold of 0.5-1.5 strain. The coefficient of friction increases linearly between the thresholds.
139 Sedimentation rates are the effective sedimentation rate computed after the model run and are thus not prescribed a priori. This
140 choice ensures that the range of average sedimentation in all our models (0.1-0.9 mm/yr) lies within observed sedimentation
141 rates in our chosen natural equivalent, the Nankai accretionary wedge in the south-western subduction margin of Japan (Korup
142 et al., 2014). Table 2 provides more details about the model run and prescribed sedimentary conditions.

143 **3. Results**

144 Subduction begins at 0.1 Myr as the weak material between continental and oceanic plate fails ([see supporting information](#)
145 [movies](#)). Continued and sustained accretion of sediments against the deforming continental crust forms the accretionary wedge
146 from the interplate contact landwards. After ~5 Myr, all models develop a distinct wedge in agreement with the critical taper
147 theory (Davis et al., 1983). Taper angles increase systematically as effective basal friction increases from $\sim 2^\circ$ to $\sim 22^\circ$ (Fig 1,
148 Table 2, $M_0^2 - M_0^{22}$). Whereas models with a relatively weaker décollement, as M_0^2 ($\phi_b = 2^\circ$), have taper slopes of $4.3^\circ \pm$



149 0.3°, models with very strong décollement, as M_0^{22} ($\phi_b = 22^\circ$), have slopes as steep as $12.8 \pm 1.2^\circ$ (Table 2). Models without
150 trench sedimentation grow solely by accretion of incoming seafloor sediments, with frequent nucleation of frontal thrusts.
151 Models with weaker décollements develop thrusts that are lengthier and remain active for shorter periods. This is clear when
152 comparing, for models with increasingly strong décollement $M_0^2 - M_0^{22}$, the average distance between first and second
153 frontal thrusts are 15.5 ± 7.0 km, 12.1 ± 3.6 km, 8.8 ± 3.3 km, 8.7 ± 2.1 km and 8.0 ± 1.8 km, respectively. Increasing
154 sedimentation rate also leads to an increase in thrust sheet length from 7.3 ± 1.1 km in $M_{0.1}^{12}$ to 13.8 ± 7.8 km in $M_{0.9}^{12}$. In
155 models with similar basal friction, models with higher sedimentation rates have lengthier thrust sheets that remain active for
156 longer periods (Table 2). Steeper surface slopes with increased décollement strengths and change in thrust sheet length with
157 sedimentation and décollement strength are well-known effects that have been confirmed by previous numerical (Mannu et
158 al., 2016; Wang & He, 1999) and analytical (Malavieille & Trullenque, 2009; Storti & McClay, 1995) models. All the reported
159 values are mean \pm Standard Deviation values recorded between 2.5-7.5 Myr in individual models. All models, exhibit a
160 temperature gradient that corresponds well with the temperature profile observed in the boreholes at IODP Site C0002 in the
161 Kumano forearc basin, on top of the Nankai accretionary wedge (Fig. S4).

162 **3.1 Thermal maturity of the wedge**

163 Sediments are more thermally mature in wedges that have a higher sedimentation rate or décollement strength. For example,
164 the mean %R₀ of simulations for wedges with the highest sedimentation ($M_{0.9}^{12}$) is 12% higher (0.75) than in those without
165 sedimentation (M_0^2) (Table 2, Fig 1). Similarly, simulations of wedges with the strongest décollement have the highest mean
166 %R₀ (0.94) of all the simulations presented in this study.

167 Thermal maturity values increase with depth and landward distance from the trench to the forearc high irrespective
168 of the décollement strength, sedimentation rates and method of thermal maturity computation (Fig. 1). As a result, sediments
169 at the core of the wedge consistently reach the highest maturity. The absolute value of %R₀ and the rate at which thermal
170 maturity values increase landward from the trench are larger for wedges with high décollement strength (Fig. 2A). In wedges
171 with the same décollement strength but higher trench sedimentation the rate of thermal maturity increase landward from the
172 trench remain very similar (Fig. 2B). Comparing the values of %R₀ (Fig. 2) along an arbitrary horizon in several models



173 emphasizes this result; the model with the highest décollement strength attains the maximum %R₀ of 1.25, and has the highest
174 rate of landward increase in thermal maturity(Fig. 2A). However, all models with similar décollement strength but different
175 sedimentation do not visibly vary in their rate or magnitude of landward increase in thermal maturity. All models show a
176 decrease in thermal maturity landward of the forearc high, commonly of 0.2 %R₀ . Other interesting observations that we
177 explore below are the increased thermal maturity occurring in the vicinity of thrusts (e.g. Fig 1) and the reversal in sediment
178 maturity around out-of-sequence thrust (e.g. Fig 1) active over longer times visible across several models (Fig 1).

179 The magnitude of %R₀ varies consistently among Easy%R₀, Simple%R₀ and Basin%R₀. On average Easy%R₀ have
180 the smallest values, followed very closely by Basin%R₀(with an average difference of only 0.02). However, Simple%R₀ had
181 the highest average value of thermal maturity being 0.16 and 0.13 higher than Easy%R₀ and Basin%R₀ (Fig 1).

182 **3.2 Sediment trajectory inside the wedge**

183 Sediments follow high-maturity paths in larger proportions in wedges with a higher décollement strength or sedimentation
184 rate. We demonstrate this effect by creating a map of the thermal maturity of sediments at 7.5 Myr of the model run, mapped
185 to their spatial position 5 Myr earlier (at 2.5 My of the model run) (Fig. 3) to analyse the spatial correlation between sediment
186 position (depth and distance) from the trench and thermal maturity. We also show the mean thermal maturity attained by
187 sediments at a given horizontal distance from the trench during this period. The scatter plot shows sharp changes with distance
188 from the trench that relate to changes in sediment trajectory (Fig. 3). The mean thermal maturity is also variable along the
189 horizontal length of the wedge and has a periodicity increasing in distance with higher sedimentation rate but relatively constant
190 with changing basal friction (Fig. 3). Whereas the mean thermal maturity has a short periodicity of ~7.2 km for the model
191 M_0^{12} with no sedimentation rates, the model $M_{0.9}^{12}$ shows the longest periodicity of 21 km. However, for all models with the
192 same no sedimentation M_0^2 - M_0^{22} the periodicity remains relatively consistent between the range of 7-8 km.

193 Fig 3 also represents the distribution of trajectories that exist in an accretionary wedge and how these trajectories get
194 impacted under trench sedimentation(a subset of these trajectories can be viewed in the supplementary Fig. S5). Whereas in
195 wedges with weak decollements (M_0^2), none of the shallowest half of incoming sediments reach %R₀ > 1 in 5 Myr, 2% of



196 sediments reach this value in wedges with strong décollement (M_0^{22}). The effects of décollement strength in the thermal
197 maturity of sediments can be quantified as well at deeper levels, with one-eighth vs more than half of the sediments surpassing
198 values of $\%R_0 = 1$ for the deepest half of incoming sediments (12.0% and 54% respectively) in weak vs strong-decollement
199 wedges (M_0^2 vs M_0^{22}), respectively. Increasing the sedimentation rate shows this effect even more prominently. In wedges
200 from the model without sedimentation (M_0^{12}), none of the top half m of sediments yield $\%R_0 > 1$, while ~ 15% of them surpass
201 $\%R_0 > 1$ in the models with a sedimentation rate of 0.9 mm/yr ($M_{0.9}^{12}$). In sum, the proportion of sediments in the top half and
202 bottom half of the wedge that reach high maturity steadily increases with both sedimentation rate and décollement strength
203 (Table 2).

204 ***3.3 Patterns of trajectory and thermal maturity in incoming sediments***

205 The diversity in the trajectory of sediments in the wedge leads to a plethora of pathways in which the sediments can become
206 thermally mature and thus introduces epistemic uncertainty in the estimation of maximum exposure temperature. Fig 4,
207 captures this uncertainty where we plot the maximum exposure temperature as a function of $\%R_0$ for all the models simulated
208 in this study. We find that almost all the models show a remarkable similarity in their relationship between maximum exposure
209 temperature and $\%R_0$ (for individual models please see Fig S6) and differ mostly in their proportion of sediments with extreme
210 values of $\%R_0$. We observe that the typical uncertainty in maximum exposure temperature increases with an increase in values
211 of $\%R_0$ with ~ 15°C interval at around $\%R_0=0.2$ compared to ~33°C interval at $\%R_0=3$ (both for 95% confidence interval,
212 Fig. 4b). Furthermore, we observe that information about the present depth of the sediments w.r.t the thickness of the wedge
213 (as represented by different colours in Fig 4a) greatly helps to further constrain the maximum exposure temperature. For
214 instance, although the overall uncertainty at $\%R_0=1$, is ~23°C, for sediments with a normalized depth of 0.2-0.4, the uncertainty
215 greatly reduces to only ~10.5°C. Thus the range of thermal maturity values for sediments clearly has a large correlation with
216 their trajectories.



217 **3.4 Comparison of Easy% R_0 , Simple% R_0 and Basin% R_0**

218 Finally as our models produced three sets of % R_0 using Easy% R_0 (referred to as $R_0\%$ throughout our study), Simple% R_0 and
219 Basin% R_0 , it also gives us a unique perspective on comparative advantages of each method. Uncertainty for all three models
220 increases with increasing % R_0 from ~20–25°C at ~0.3 which rises to ~35°C at $R_0\%=3.5$ (Fig 4b). Easy% R_0 is the most well-
221 recognised method of thermal maturity computation and yields the best constraint on uncertainty for very small changes
222 around the values less than 1. For the values of % R_0 between 1 and 3, all models yield very similar uncertainty, with
223 Simple% R_0 yielding the most constrained exposure temperatures(Fig 4b). However, beyond $R_0\%=3$, the Simple% R_0 becomes
224 highly unreliable, with uncertainty in exposure temperatures as high as 55°C at $R_0\%=4$. Easy% R_0 yields a reasonable
225 uncertainty range of ~37°C till $R_0\%=4.4$, but starts to be unreliable above this value. Basin% R_0 remains consistent till a very
226 high value of $R_0\%$ (~6), and thus provides the best constraint on the widest range of values of thermal maturity(Fig 4b).

227

228 **4. Discussion**

229 Our models achieve realistic thermal maturity distributions thanks to unique computational advantages over models in the
230 previous studies(Mannu et al., 2016, 2017; Miyakawa et al., 2019), despite several relevant assumptions. Models are simplified
231 by assuming no elasticity, predefined décollement, no erosion, and using simple and uniform rheology, and either has an
232 insufficient resolution or lack empirical relations to simulate the compaction of sediments and processes of multiscale fluid
233 flow. Although these assumptions hinder a wholesale comparison between our simulations and natural examples of
234 accretionary wedges, we are confident of the thermal maturity patterns of our models. Our estimated % R_0 values for the model
235 $M_{0.1}^{12} - M_{0.9}^{12}$ are in very good agreement with the % R_0 values measured for the borehole C0002 Nankai accretionary wedge
236 (used for thermal conductivity values) by Fukuchi et. al. 2009 (Figure 5). Moreover, the temperature estimated from the
237 observed thermal maturity of a timeframe of 1-2 Myr in the borehole, also strongly correlates with the trend and the range of
238 95% Confidence interval of T vs % R_0 estimated in our models (Fig S7). Furthermore, our models also correlate with the
239 patterns of P-wave velocity for Nankai(Górszczyk et al., 2019; Nakanishi et al., 2018) and Hikurangi(Arai et al., 2020)
240 margins(Dewing & Sanei, 2009). Models compute realistic thermal maturity distributions thanks to several key improvements.



241 Firstly, our models calculate temperature gradients that evolve at long time intervals and thus closely replicate accretionary
242 wedges in nature (Fig. S2). This enables the simulation of realistic temperature profiles based on thermal conductivity values
243 derived empirically from natural accretionary wedges, as in our case, the Nankai margin (Sugihara et al., 2014) Secondly, our
244 simulations account for the effects that thermal and isostatic feedback from the oceanic lithosphere have on the evolution of
245 the wedge by simulating plate subduction at a large scale rather than just the accretionary wedge (Miyakawa et al., 2019).
246 Finally, our method calculates the vitrinite reflectance of sediments on each marker of the model. This capacity to accurately
247 estimate thermal maturity in each marker informs the research questions of this study and allows inferences beyond those of
248 depth-dependent thermal maturity distributions.

249 The thermal maturity of the wedge increases landward, as signalled by the landward increase in %R₀ (Fig. 1). This
250 has been observed in natural accretionary wedges such as Miura–Boso plate subduction margin (Yamamoto et al., 2017), fold
251 and thrust belts Western Foothills complex in western Taiwan (Arito Sakaguchi et al., 2007) and other numerical models of
252 accretion (Miyakawa et al., 2019), resulting from the long-term deformation of older accreted sediments and the backstop-
253 forced exhumation in the wedge. Our models show that the rate of landward rise in thermal maturity is faster for thicker wedges
254 (Fig 2). This is the case for wedges with high basal strength (M_0^{22}), for sediments in thicker wedges deform more prominently
255 than those in their thinner counterparts. Simulations also show that sediments reach deeper levels in thicker wedges and that
256 this increases the overall thermal maturity of the wedge. Also, increased exhumation rates and steeper thermal maturity
257 gradients occur in the wedge interior, as the continental backstop deflects sediment trajectories upwards during accretion (Fig.
258 2). As a result, for the geometry of the backstop used in our models, backstop-forced exhumed material is, on average,
259 thermally more mature.

260 Our models expose two relevant cases where the increase of thermal maturity with depth or landward is relevantly
261 altered: on-fault increase and fault-block inversion. Our models attest to the steep rise in thermal maturity of sediments at fault
262 sites (Fig. 1). This is well documented in nature, as for boreholes C0004 (Sakaguchi et al., 2011). However, on-fault increases
263 in thermal maturity are comparatively smaller in our simulations and lack the marked increase in %R₀ observed at fault sites
264 in nature. This is primarily due to our models developing wider fault zones than their natural equivalents and the subsequent
265 acceleration in the thermal diffusion occurring in simulated thrusts. During fault-block inversions, the positive gradient of



266 thermal maturity with depth is inverted by thrusting relatively mature sediments over less mature sediments(Underwood et al.,
267 1992). This is known from natural observations, as along the Fukase Fault in Shimanto accretionary wedge(Ohmori et al.,
268 1997) and underneath the forearc basin in Nankai accretionary wedge(Fukuchi et al., 2017), and previous modelling
269 efforts(Miyakawa et al., 2019).

270 Collation of the above implies that the thermal maturity of accretionary wedges results from the general increase of
271 thermal maturity (i) with depth and (ii) landward, as well as from its (iii) modification by thrust faults. Our models suggest
272 thermal maturity inversions by thrusting, which are commonplace in accretionary contexts, are the primary cause of thermal
273 maturity differentiation among wedges with initially similar geothermal gradients. In other words, the strong differentiation in
274 the trajectory of sediments led by thrusting has a larger influence over thermal maturity than burial depth or in-wedge location.
275 This novel inference has probably remained concealed thus far due to the large number of parameters that condition thrust
276 development, frequency, length, and thermal state. Influencing parameters to include sedimentation, erosion, basal friction and
277 relief, pore pressure and fluid state, wedge length and thickness, taper angle, and many others(Dominguez et al., 2000; E.
278 Konstantinovskaia, 2005; Mannu et al., 2016; Ruh, 2017; Simpson, 2010; H. J. Tobin & Saffer, 2009). It is nevertheless
279 important to note that the frequency of faults in a wedge can be impacted by many other factors, including hinterland
280 sedimentation(Simpson, 2010; Storti & Mcclay, 1995), erosion(E. Konstantinovskaia, 2005; S. D. Willett, 1999), and seafloor
281 topography(Dominguez et al., 2000). Below, we discuss how thrusts not only alter the thermal evolution of accreting sediments
282 but are, in fact, the primary control of their thermal maturity.

283 Thermal maturity correlates with sediment depth weakly near faults and more strongly away from them. The distance
284 of sediment from frontal thrust dictates the trajectory of sediment grains, and as a result, the pressure-temperature conditions
285 to which they are exposed. In this study, we have considered solely how décollement strength and the rate of trench
286 sedimentation vary the frequency, architecture, and overall behaviour of thrusts, and the frontal thrust, as the wedge evolves.
287 Our results show the need to consider all factors influencing fault frequency when inferring the geothermal history of
288 contractional terrains by means of thermal maturity. Fortunately, this predictive exercise should be relatively straightforward,
289 for the impact of these external factors on the fault structure of wedges has been established(Fillon et al., 2012; Mannu et al.,



290 2016, 2017; Mugnier et al., 1997; Simpson, 2010; Storti & Mcclay, 1995), and the effect of each of these factors can be
291 accounted for when assessing the trajectory of sediments and the distribution of thermal maturity in accretionary wedges.

292 Sediment mixing in subduction wedges is primarily controlled by thrusting. Previous studies have reached seemingly
293 contradicting outcomes when using numerical(Miyakawa et al., 2019; Wenk & Huhn, 2013; S. Willett et al., 1993) and
294 analogue(E. Konstantinovskaia, 2005; Mulugeta & Koyi, 1992) approaches to analyze sediment trajectories as a function of
295 changes in erosion, sedimentation, or décollement strength. While some studies showed that the rate and extent of a transition
296 by which sediment trajectories change from generally horizontal to increasingly vertical during accretion change consistently
297 with the initial depth of incoming sediments(Mulugeta & Koyi, 1992; S. Willett, 1992), others predicted different crossover
298 paths for sediments accreting over a range of décollement strengths(E. Konstantinovskaia, 2005). Our models show that both
299 are valid results and that changes in trajectory patterns leading to path crossovers are controlled by the horizontal distance of
300 sediments from the frontal thrust. Starting at a threshold distance from the trench, sediments at different depths follow laminar
301 paths along different trajectories within the wedge. Laminar-type trajectories can be reproduced in a broad range of simulations
302 and are particularly common in models with low sedimentation and décollement strengths. However, the depth dependence of
303 sedimentary paths varies periodically as a function of distance from the trench of specific sedimentary packages (Fig. 3,6).
304 This effect, which is particularly marked in the neighbourhood of the frontal thrust, explains the crossover paths for incoming
305 sedimentary packages at similar depths and different horizontal locations, as shown by Konstantinovskaia et al. 2005.
306 Therefore, thrust faults in the wedge act as the primary agent controlling whether sediments sustain depth-controlled laminar
307 flow or mix.

308 The thermal maturity that incoming sediments reach varies periodically as a function of thrust frequency. Although
309 previous research considered non-laminar sediment trajectories as chaotic(Mary et al., 2013), and the wide variety of
310 trajectories shown in our models seem to agree with this (Fig 3, Fig S4), patterns emerge when we correlate the lateral and
311 vertical position of incoming sediments with their eventual thermal maturity. Changes in the depth of the thermal maturity
312 boundary are less frequent and have larger amplitudes with increased décollement strength, and especially, increased
313 sedimentation rates (Fig. 4). The periodicity in the thermal maturity boundary marks the periodic oscillation of the predominant
314 trajectory followed by incoming sediments, i.e., between accretion (low thermal maturity path) and underthrusting (high-



315 thermal maturity path). As a result, it should also strongly correlate with the periodicity observed in the evolution of forearc
316 topography (Menant et al., 2020) and the frequency of thrust formation as such in our models. This is expected, given that
317 thrusts are active over longer mean times, and they thus channel material toward the décollement more efficiently, in wedges
318 with stronger décollement or increased sedimentation. While sediments at internal and higher structural positions of the wedge
319 are translated towards the surface and have a lower thermal maturity, sediments at external and lower structural positions are
320 translated towards the décollement and have a relatively higher maturity. This is a relevant observation, for it typifies the
321 causality of particular sediment grains following a high or low maturity path, a long-standing unanswered question (Miyakawa
322 et al., 2019). We corroborate this observation by analyzing the terminal thermal maturity of sediments across a frontal thrust
323 active at a younger age. For example, by showing the thermal maturity of sediments at ~7.5 Myr across a thrust active at ~4
324 Myr, as in Fig. 7. Whereas this occurs for all thrusts in the wedge, the frontal thrust is particularly pronounced in partitioning
325 sediments into the high and low maturity paths.

326 Geothermal information stored in the incoming sediments can only be retrieved if sediments are at appropriate
327 locations with respect to emergent thrusts. We illustrate this using two runs of the same model and tracking an artificial thermal
328 anomaly imposed on incoming sediments at two different locations (Fig. 7). This hypothetical thermal anomaly can be
329 conceptualized as any alteration of the thermal maturity profile of incoming sediments, for example, elevated heat flows by an
330 antecedent magmatic intrusion. While the change in % R_0 associated with the short-lived thermal anomaly results in abnormally
331 high values of thermal maturity in both sediment packages, it can only be retrieved for the end-model run of sediments located
332 further from the trench (those in the right panel, Fig. 7b). Contrarily, the end-model run of sediments closer to the trench (those
333 in the left panel, Fig. 7a) shows no signs of discontinuity in the thermal maturity distribution of the wedge. This is because we
334 deliberately placed the thermal anomaly at sites that evolve at two structural locations during the model run, i.e., above and
335 below a yet-undeveloped frontal thrust (Fig. 7). The sediment sector affected by the thermal anomaly closer to the trench is
336 overthrust by the frontal thrust and remains in a footwall location thereafter (Fig. 7a). In contrast, the homologous
337 sedimentary package further away from the trench is accreted by the frontal thrust and remains in a hanging-wall location (Fig.
338 7b). Thus, the preservation of the record of an antecedent thermal anomaly is only possible in the former case. We further note
339 that, in our simulations, the entire vertical column of sediments records the thermal anomaly, while in nature, the anomaly may



340 affect only sediments at the deeper locations of the sedimentary pile, which are in turn the sediments that most likely to follow
341 a high-maturity path. We thus regard the possibility of retrieving such antecedent geothermal information as minimal.

342 The main implications of this contribution emerge from its predictive power. Our approach can predict to a precise the thermal
343 maturity of sediments and the uncertainty associated with the maximum exposure temperature in accretionary contexts with
344 known structuration. More accurate quantification of the thermal evolution and thermal state of accreted sediments reduces
345 the uncertainties attached to the location of temperature-led transformations of organic material into hydrocarbons in
346 subduction margins and other accretionary contexts. Such increased accuracy in the distribution of thermally mature sediments
347 may also be applied for improved assessments of the evolution in time of any other geothermal process, including seismic slip,
348 magmatic and metamorphic extent, porosity, compaction and diagenesis of sediments, and the reconstruction of convergent
349 margins in general (Bostick & Pawlewicz, 1984; Ferreiro Mählmann & Le Bayon, 2016; Rabinowitz et al., 2020; A. Sakaguchi
350 et al., 2011; Totten & Blatt, 1993; Underwood et al., 1992).

351 Finally, among the three methods of R_0 computation, Easy R_0 and Basin R_0 are clearly more consistent and well-
352 constrained on a wide range of thermal maturity in comparison to Simple R_0 , which seems to be particularly useful for a
353 smaller range of thermal maturity values. This simply illustrates the fact that while Easy R_0 and Basin R_0 computation
354 deals with several parallel reactions related to the maturity of kerogen (and hence multiple activation energies), the Simple R_0
355 is based on best-fitted single activation energy, and hence yields large confidence intervals at the extreme R_0 values.
356 Additionally, the inclusion of the higher activation energy reactions in Basin R_0 makes it the best-suited formulation for
357 sediments at the deeper and shear zone sediments which usually get saturated using Easy R_0 .

358 **4. Conclusion**

359 This study demonstrates how contractional faults alter the paths of sediments as they accrete and how this fundamentally
360 controls the distribution of the thermal maturity of sediments in accretionary wedges and emphasizes the role that
361 sedimentation rate and interplate contact strength have in such distribution. The increased resolution of our approach leads to
362 findings that have relevant implications. For example, the geothermal history that can be retrieved from the thermal maturity
363 of sediments in drills, i.e., at the shallow wedge, provides, at best, an incomplete record that is skewed towards the thermal



364 evolution of sediments near the trench. Coevally, relevant sectors of sediments located further seaward, when not subducted,
365 follow high-maturity paths that overprint their antecedent thermal history. Finally, this study also provides a first-order
366 uncertainty measure for the thermal maturity of sediments based on the diversity in their trajectory.

367 **Competing interests**

368 The authors declare that they have no conflict of interest.

369 **References**

- 370 Arai, R., Kodaira, S., Henrys, S., Bangs, N., Obana, K., Fujie, G., et al. (2020). Three-dimensional P wave velocity
371 structure of the northern hikurangi margin from the NZ3D experiment: Evidence for fault-bound anisotropy. *Journal of*
372 *Geophysical Research, [Solid Earth]*, 125(12). <https://doi.org/10.1029/2020jb020433>
- 373 Argo. (2022). Argo float data and metadata from Global Data Assembly Centre (Argo GDAC) [Data set]. SEANOE.
374 <https://doi.org/10.17882/42182>
- 375 Bostick, N. H., & Pawlewicz, M. J. (1984). Paleotemperatures based on vitrinite reflectance of shales and limestone in
376 igneous dike aureoles in the Upper Cretaceous Pierre shale, Walsenburg, Colorado. Retrieved from
377 <http://archives.datapages.com/data/rmag/SourceRocks84/bostick.pdf>
- 378 Burg, J.-P., & Gerya, T. V. (2005). The role of viscous heating in Barrovian metamorphism of collisional orogens:
379 thermomechanical models and application to the Lepontine Dome in the Central Alps. *Journal of Metamorphic*
380 *Geology*, 23(2), 75–95.
- 381 Burnham, A. K., & Sweeney, J. J. (1989). A chemical kinetic model of vitrinite maturation and reflectance.
382 *Geochimica et Cosmochimica Acta*, 53(10), 2649–2657.
- 383 Byrne, T., & Fisher, D. (1990). Evidence for a weak and overpressured décollement beneath sediment-dominated
384 accretionary prisms. *Journal of Geophysical Research*. <https://doi.org/10.1029/jb095ib06p09081>
- 385 Davis, D., Suppe, J., & Dahlen, F. A. (1983). Mechanics of fold-and-thrust belts and accretionary wedges. *Journal of*
386 *Geophysical Research*. <https://doi.org/10.1029/JB088iB02p01153>
- 387 Dewing, K., & Sanei, H. (2009). Analysis of large thermal maturity datasets: Examples from the Canadian Arctic
388 Islands. *International Journal of Coal Geology*, 77(3), 436–448.



- 389 Dominguez, S., Malavieille, J., & Lallemand, S. E. (2000). Deformation of accretionary wedges in response to
390 seamount subduction: Insights from sandbox experiments. *Tectonics*, *19*(1), 182–196.
- 391 Ferreiro Mählmann, R., & Le Bayon, R. (2016). Vitrinite and vitrinite like solid bitumen reflectance in thermal
392 maturity studies: Correlations from diagenesis to incipient metamorphism in different geodynamic settings.
393 *International Journal of Coal Geology*, *157*, 52–73.
- 394 Fillon, C., Huisman, R. S., & van der Beek, P. (2012). Syntectonic sedimentation effects on the growth of fold-and-
395 thrust belts. *Geology*, *41*(1), 83–86.
- 396 Fukuchi, R., Yamaguchi, A., Yamamoto, Y., & Ashi, J. (2017). Paleothermal structure of the Nankai inner
397 accretionary wedge estimated from vitrinite reflectance of cuttings. *Geochemistry, Geophysics, Geosystems*, *18*(8),
398 3185–3196.
- 399 Gerya, T. (2019). *Introduction to Numerical Geodynamic Modelling*. Cambridge University Press.
- 400 Gerya, T. V., & Yuen, D. A. (2003). Characteristics-based marker-in-cell method with conservative finite-differences
401 schemes for modeling geological flows with strongly variable transport properties. *Physics of the Earth and Planetary*
402 *Interiors*, *140*(4), 293–318.
- 403 Giunchi, C., & Ricard, Y. (1999). High-pressure/low-temperature metamorphism and the dynamics of an accretionary
404 wedge. *Geophysical Journal International*, *136*(3), 620–628.
- 405 Górszczyk, A., Operto, S., Schenini, L., & Yamada, Y. (2019). Crustal-scale depth imaging via joint full-waveform
406 inversion of ocean-bottom seismometer data and pre-stack depth migration of multichannel seismic data: a case study
407 from the eastern Nankai Trough. *Solid Earth*, *10*(3), 765–784.
- 408 Hori, T., & Sakaguchi, H. (2011). Mechanism of décollement formation in subduction zones. *Geophysical Journal*
409 *International*, *187*(3), 1089–1100.
- 410 Konstantinovskaia, E. (2005). Erosion and exhumation in accretionary orogens: Experimental and geological
411 approaches. *Geochemistry, Geophysics, Geosystems*. Retrieved from
412 <https://agupubs.onlinelibrary.wiley.com/doi/abs/10.1029/2004GC000794>
- 413 Konstantinovskaia, E., & Malavieille, J. (2005). Erosion and exhumation in accretionary orogens: Experimental and
414 geological approaches. *Geochemistry, Geophysics, Geosystems*. <https://doi.org/10.1029/2004gc000794>



- 415 Korup, O., Hayakawa, Y., Codilean, A. T., Matsushi, Y., Saito, H., Oguchi, T., & Matsuzaki, H. (2014). Japan's
416 sediment flux to the Pacific Ocean revisited. *Earth-Science Reviews*, *135*, 1–16.
- 417 Luján, M., Rossetti, F., Storti, F., Ranalli, G., & A. Socquet. (2010). Flow trajectories in analogue viscous orogenic
418 wedges: Insights on natural orogens. *Tectonophysics*, *484*(1), 119–126.
- 419 Malavieille, J., & Trullenque, G. (2009). Consequences of continental subduction on forearc basin and accretionary
420 wedge deformation in SE Taiwan: Insights from analogue modeling. *Tectonophysics*, *466*(3), 377–394.
- 421 Mannu, U., Ueda, K., Willett, S. D., Gerya, T. V., & Strasser, M. (2016). Impact of sedimentation on evolution of
422 accretionary wedges: Insights from high-resolution thermomechanical modeling. *Tectonics*.
423 <https://doi.org/10.1002/2016tc004239>
- 424 Mannu, U., Ueda, K., Willett, S. D., Gerya, T. V., & Strasser, M. (2017). Stratigraphic signatures of forearc basin
425 formation mechanisms. *Geochemistry, Geophysics, Geosystems*, *18*(6), 2388–2410.
- 426 Mary, B. C. L., Maillot, B., & Leroy, Y. M. (2013). Deterministic chaos in frictional wedges revealed by convergence
427 analysis. *International Journal for Numerical and Analytical Methods in Geomechanics*.
428 <https://doi.org/10.1002/nag.2177>
- 429 Menant, A., Angiboust, S., Gerya, T., Lacassin, R., Simoes, M., & Grandin, R. (2020). Transient stripping of
430 subducting slabs controls periodic forearc uplift. *Nature Communications*, *11*(1), 1823.
- 431 Miyakawa, A., Kinoshita, M., Hamada, Y., & Otsubo, M. (2019). Thermal maturity structures in an accretionary wedge
432 by a numerical simulation. *Progress in Earth and Planetary Science*, *6*(1), 8.
- 433 Mugnier, J. L., Baby, P., Colletta, B., Vinour, P., Bale, P., & Leturmy, P. (1997). Thrust geometry controlled by
434 erosion and sedimentation: A view from analogue models. *Geology*, *25*(5), 427–430.
- 435 Mulugeta, G., & Koyi, H. (1992). Episodic accretion and strain partitioning in a model sand wedge. *Tectonophysics*,
436 *202*(2), 319–333.
- 437 Nakanishi, A., Takahashi, N., Yamamoto, Y., Takahashi, T., Citak, S. O., Nakamura, T., et al. (2018). Three-
438 dimensional plate geometry and P-wave velocity models of the subduction zone in SW Japan: Implications for
439 seismogenesis. *Geology and Tectonics of Subduction Zones: A Tribute to Gaku Kimura: Geological Society of America*
440 *Special Paper*, *534*, 69–86.



- 441 Ohmori, K., Taira, A., Tokuyama, H., Sakaguchi, A., Okamura, M., & Aihara, A. (1997). Paleothermal structure of the
442 Shimanto accretionary prism, Shikoku, Japan: Role of an out-of-sequence thrust. *Geology*, 25(4), 327–330.
- 443 Platt, J. P. (1986). Dynamics of orogenic wedges and the uplift of high-pressure metamorphic rocks. *GSA Bulletin*,
444 97(9), 1037–1053.
- 445 Platt, J. P. (1993). Exhumation of high-pressure rocks: a review of concepts and processes. *Terra Nova*, 5(2), 119–133.
- 446 Quigley, T. M., & Mackenzie, A. S. (1988). The temperatures of oil and gas formation in the sub-surface. *Nature*,
447 333(6173), 549–552.
- 448 Rabinowitz, H. S., Savage, H. M., Polissar, P. J., Rowe, C. D., & Kirkpatrick, J. D. (2020). Earthquake slip surfaces
449 identified by biomarker thermal maturity within the 2011 Tohoku-Oki earthquake fault zone. *Nature Communications*,
450 11(1), 533.
- 451 Ranalli, G. (1995). *Rheology of the Earth*. Springer Science & Business Media.
- 452 Ruh, J. B. (2017). Effect of fluid pressure distribution on the structural evolution of accretionary wedges. *Terra Nova*,
453 29(3), 202–210.
- 454 Ruh, J. B. (2020a). Numerical modeling of tectonic underplating in accretionary wedge systems. *Geosphere*, 16(6),
455 1385–1407.
- 456 Ruh, J. B. (2020b). Numerical modelling of tectonic underplating in accretionary wedges (p. 5607).
- 457 Sakaguchi, A., Yanagihara, A., Ujiie, K., Tanaka, H., & Kameyama, M. (2007). Thermal maturity of a fold–thrust belt
458 based on vitrinite reflectance analysis in the Western Foothills complex, western Taiwan. *Tectonophysics*, 443(3), 220–
459 232.
- 460 Sakaguchi, A., Chester, F., Curewitz, D., Fabbri, O., Goldsby, D., Kimura, G., et al. (2011). Seismic slip propagation to
461 the updip end of plate boundary subduction interface faults: Vitrinite reflectance geothermometry on Integrated Ocean
462 Drilling Program NanTro SEIZE cores. *Geology*. <https://doi.org/10.1130/g31642.1>
- 463 Schmoker, J. W., & Gautier, D. L. (1988). Sandstone porosity as a function of thermal maturity. *Geology*, 16(11),
464 1007–1010.
- 465 Simpson, G. D. H. (2010). Formation of accretionary prisms influenced by sediment subduction and supplied by
466 sediments from adjacent continents. *Geology*, 38(2), 131–134.



- 467 Storti, F., & McClay, K. (1995). Influence of syntectonic sedimentation on thrust wedges in analogue models.
468 [https://doi.org/10.1130/0091-7613\(1995\)023<0999](https://doi.org/10.1130/0091-7613(1995)023<0999)
- 469 Sugihara, T., Kinoshita, M., Araki, E., Kimura, T., Kyo, M., Namba, Y., et al. (2014). Re-evaluation of temperature at
470 the updip limit of locked portion of Nankai megasplay inferred from IODP Site C0002 temperature observatory. *Earth,*
471 *Planets and Space.* <https://doi.org/10.1186/1880-5981-66-107>
- 472 Tesei, T., Lacroix, B., & Collettini, C. (2015). Fault strength in thin-skinned tectonic wedges across the smectite-illite
473 transition: Constraints from friction experiments and critical tapers. *Geology*, *43*(10), 923–926.
- 474 Tissot, B. P., & Welte, D. H. (2013). *Petroleum Formation and Occurrence.* Springer Science & Business Media.
- 475 Tissot, B. P., Pelet, R., & Ungerer, P. H. (1987). Thermal History of Sedimentary Basins, Maturation Indices, and
476 Kinetics of Oil and Gas Generation. *AAPG Bulletin*, *71*(12), 1445–1466.
- 477 Tobin, H., Hirose, T., Saffer, D., Toczko, S., Maeda, L., Kubo, Y., et al. (2015). Site C0002. *Proceedings of the IODP.*
478 <https://doi.org/10.2204/iodp.proc.348.103.2015>
- 479 Tobin, H. J., & Saffer, D. M. (2009). Elevated fluid pressure and extreme mechanical weakness of a plate boundary
480 thrust, Nankai Trough subduction zone. *Geology*, *37*(8), 679–682.
- 481 Totten, M. W., & Blatt, H. (1993). Alterations in the non-clay-mineral fraction of pelitic rocks across the diagenetic to
482 low-grade metamorphic transition, Ouachita Mountains, Oklahoma and Arkansas. *Journal of Sedimentary Research*,
483 *63*(5), 899–908.
- 484 Underwood, M. B., Laughland, M. M., Byrne, T., Hibbard, J. P., & DiTullio, L. (1992). Thermal evolution of the
485 Tertiary Shimanto Belt, Muroto Peninsula, Shikoku, Japan. *The Island Arc.* <https://doi.org/10.1111/j.1440->
486 [1738.1992.tb00064.x](https://doi.org/10.1111/j.1440-1738.1992.tb00064.x)
- 487 Wang, K., & He, J. (1999). Mechanics of low-stress forearcs: Nankai and Cascadia. *Journal of Geophysical Research,*
488 *[Solid Earth]*, *104*(B7), 15191–15205.
- 489 Waples, D. W. (1981). *Organic Geochemistry for Exploration Geologists.* Springer Netherlands.
- 490 Wenk, L., & Huhn, K. (2013). The influence of an embedded viscoelastic–plastic layer on kinematics and mass
491 transport pattern within accretionary wedges. *Tectonophysics*, *608*, 653–666.
- 492 Willett, S. (1992). Dynamic and kinematic growth and change of a Coulomb wedge. *McClay, K. R.*, 19–31.



493 Willett, S., Beaumont, C., & Fullsack, P. (1993). Mechanical model for the tectonics of doubly vergent compressional
 494 orogens. *Geology*. [https://doi.org/10.1130/0091-7613\(1993\)021<0371:MMFTTO>2.3.CO](https://doi.org/10.1130/0091-7613(1993)021<0371:MMFTTO>2.3.CO)

495 Willett, S. D. (1999). Orogeny and orography: The effects of erosion on the structure of mountain belts. *Journal of*
 496 *Geophysical Research*, *104*, 28957.

497 Yamamoto, Y., Hamada, Y., Kamiya, N., Ojima, T., Chiyonobu, S., & Saito, S. (2017). Geothermal structure of the
 498 Miura–Boso plate subduction margin, central Japan. *Tectonophysics*, *710-711*, 81–87.

499
500
501
502
503
504
505
506

507 **List of Tables**

508 **Table 1: Properties for the different materials used for the model runs**

Rock Type	Density (kg/m ³)	Cohesion (MPa)	Coefficient of friction(μ)	Thermal Conductivity (W/(m K))	Flow law	E (kJ/mol)	n
Water	1000	0	0	20		0	0
Air (Sticky-air)	0	0	0	20		0	0
Décollement	2600	0.001	0.03 / 0.08	$(1.5+807/(T+77))^*$ $(1-\exp(-Z^2/1.3e7))$	Wet quartzite	154	2.3
Sediments1	2600	0.5/0.05*	4.64/0.2*	$(0.96+807/(T+77))^*$ $(1-\exp(-Z^2/1.3e7))$	Wet quartzite	154	2.3



Sediments2	2600	0.5/0.05*	4.64/0.2*	$(0.96+807/(T+77))^* (1-\exp(-Z^2/1.3e7))$	Wet quartzite	154	2.3
Upper Continental Crust	2700	1	0.6	$0.64+807/(T+77)$	Wet quartzite	300	2.3
Lower Continental Crust	2800	1	0.6	$0.64+807/(T+77)$	Wet quartzite	300	3.2
Upper Oceanic Crust	3000	1	0.6	$1.18+474/(T+77)$	Plagioclase An75	300	2.3
Lower Oceanic Crust	3000	1	0.6	$1.18+474/(T+77)$	Plagioclase An75	300	3.2
Mantle Lithosphere	3300	1	0.6	$0.73+1293/(T+77)$	Dry olivine	532	3.5
Asthenosphere	3300	1	0.6	$0.73+1293/(T+77)$	Dry olivine	532	3.5

*Strain-softened Cohesion/Coefficient of friction
 T is Temperature, Z is the depth from the seafloor.

509

510



511 **Table 2: Model runs and their specific characteristic observations**

Models	φ_b	φ / φ_{ss}	SR	L	α	D	$\langle R_o \% \rangle$	% _{top-half}	% _{Bottom-half}
M_0^2	2°	30°/15°	None	123.2±15.7	4.3±0.3°	15.5±7.0	0.54	0.0	12.7
M_0^7	7°	30°/15°	None	97.7±9.9	6.5±0.5°	12.1±3.6	0.60	0.0	22.5
M_0^{12}	12°	30°/15°	None	77.8±4.8	8.9±0.5°	8.7±2.1	0.67	0.0	31.3
$M_{0.1}^{12}$	12°	30°/15°	0.1	76.1±5.9	8.9±0.9°	7.3±1.1	0.71	0.1	35.3
$M_{0.3}^{12}$	12°	30°/15°	0.3	79.3±8.2	8.6±1.3°	7.8±2.5	0.69	0.1	32.0
$M_{0.5}^{12}$	12°	30°/15°	0.5	79.9±7.4	8.5±0.6°	9.5±4.0	0.71	2.7	34.4
$M_{0.7}^{12}$	12°	30°/15°	0.7	81.3±10.5	8.5±1.0°	9.9±5.0	0.73	4.2	41.5
$M_{0.9}^{12}$	12°	30°/15°	0.9	82.5±11.0	8.8±1.5°	13.8±7.8	0.75	14.6	51.8
M_0^{17}	17°	30°/15°	None	71.6±5.0	10.7±0.8°	8.8±3.3	0.83	1.2	40.6
M_0^{22}	22°	30°/15°	None	62.7±6.0	12.8±1.2°	8.0±1.8	0.94	2.0	54.0

φ_b is décollement Strength (internal angle of friction)

φ Sediment Strength

φ_{ss} Sediment Strength (Strain weakened)/(internal angle of friction)

SR Average Sediment rate (mm/yr)

L Average Length (in km) between ~2.5-7.5Myr

α Average Taper angle α (in degrees) between ~2.5-7.5Myr

D Average Distance between the first and second frontal thrust between ~2.5-7.5Myr(in km)

T Average time a frontal thrust remains active between ~3.5-7.5Myr

$\langle R_o \% \rangle$ Average vitrinite reflectance of the wedge between ~3.5-7.5 Myr

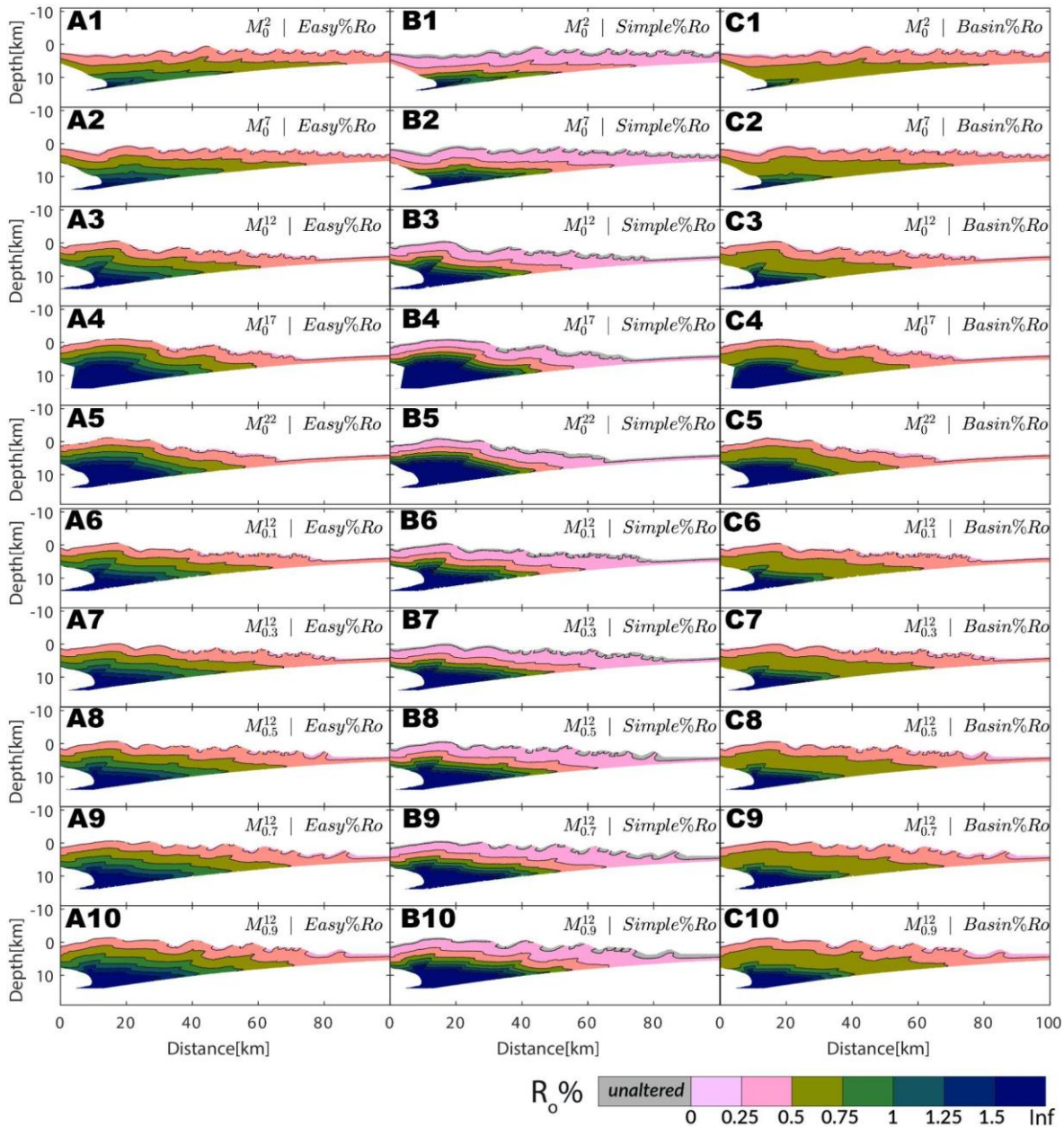
%_{top} Proportion of >1 eventual $R_o\%$ (*vitrinite reflectance at 7.5 Myr*) at shallow half of the incoming sediment at 2.5 Myr.

%_{bottom} Proportion of >1 eventual $R_o\%$ (*vitrinite reflectance at 7.5 Myr*) at deep half of the concoming sediments.



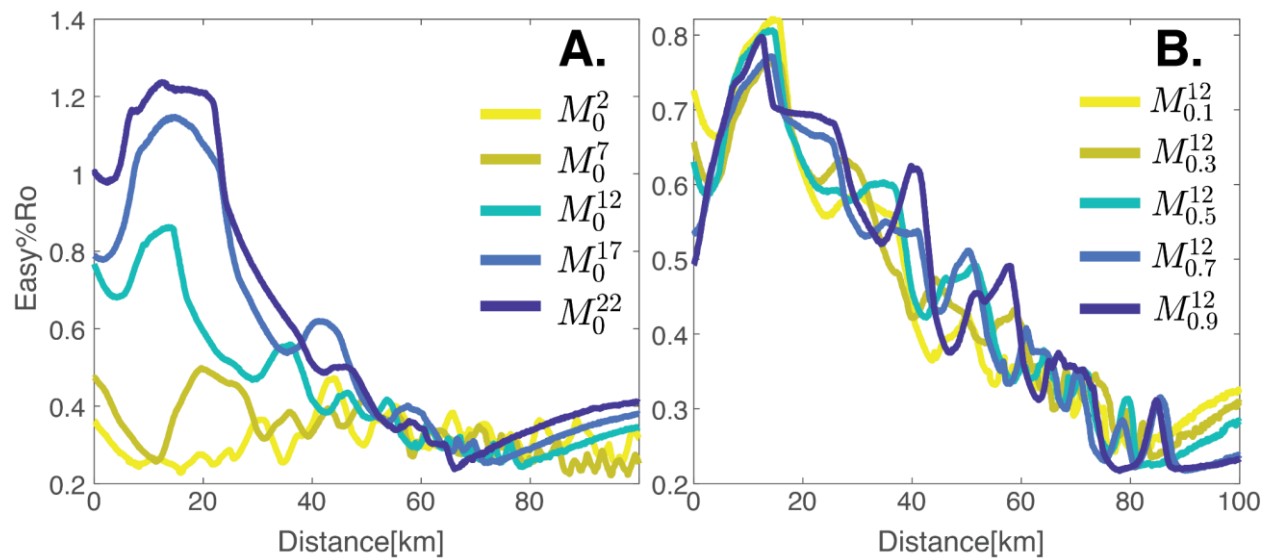
512 **List of Figures**

513 **Fig. 1:** Distribution of thermal maturity for different models at ~7.5 Myr (5 Myr of thermal maturation). Panels A1-A5 show
 514 the thermal maturity distribution (computed using Easy%Ro) in subduction wedges of models as a function of décollement
 515 strength $M_0^2 - M_0^{22}$, respectively. A6-A10 show the thermal maturity distribution in subduction wedges of models function
 516 of sedimentation rate $M_{0.1}^{12} - M_{0.9}^{12}$, respectively. The grey color of the markers indicate that no thermal maturity change in
 517 these sediments have not occurred. B1-B10 and C1-C10 similarly show the thermal maturity distribution in subduction wedges
 518 computed using Simple%Ro and Basin%Ro, respectively.





520 **Fig. 2:** The variation of % R_0 for an horizon at the trench depth of each model at 7.5 Myr. Panel A shows all the models with
521 different decollement stretch (M_0^2 - M_0^{22}). Panel B shows all the models with different sedimentation rates ($M_{0.1}^{12}$ - $M_{0.9}^{12}$)

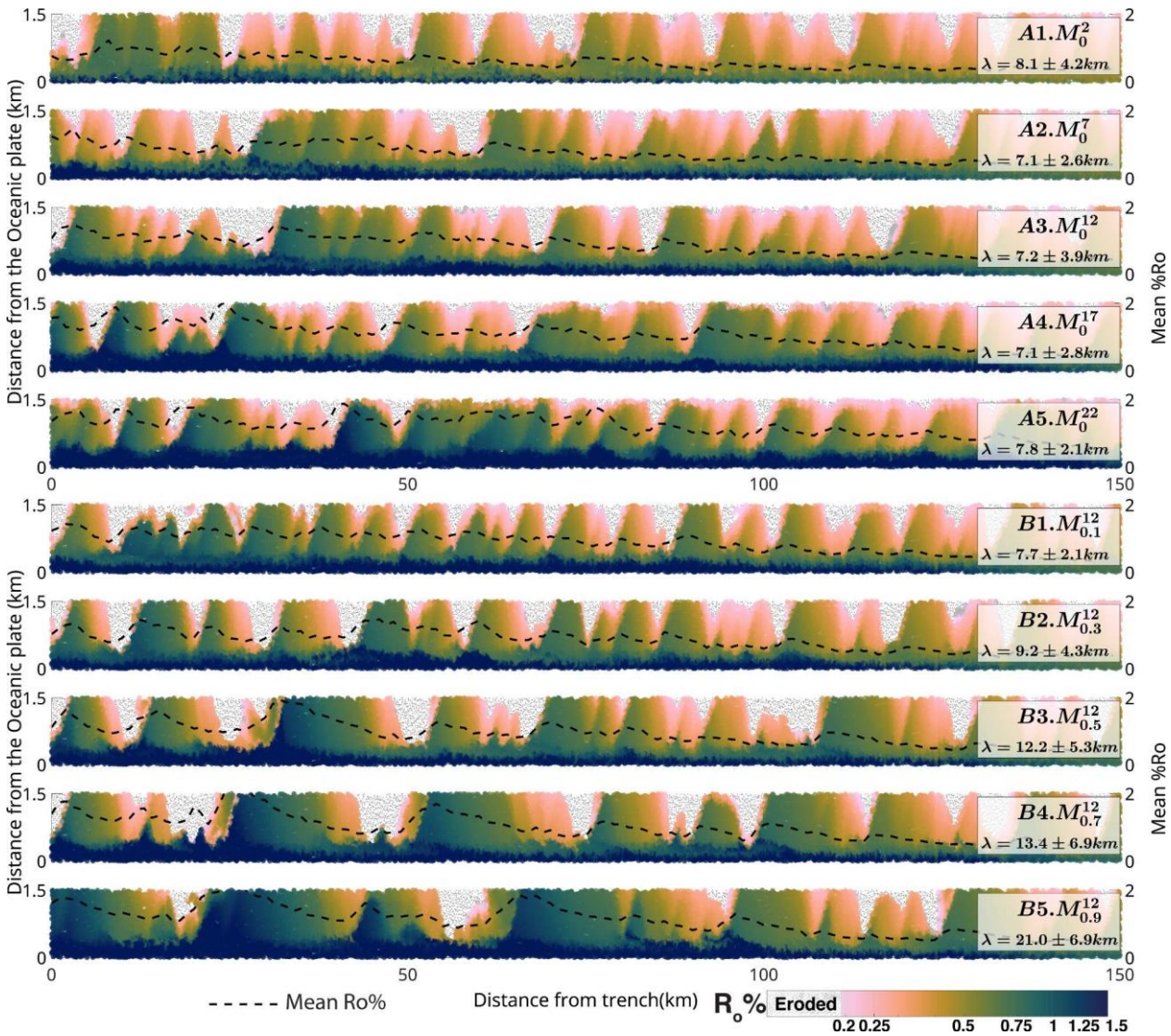


522



523
 524
 525
 526
 527
 528
 529

Fig. 3: Map of thermal maturity at 7.5 Myr mapped to sediments at 2.5 Myr. Panel A1-A5, B1-B5 show the mapping for models M_0^2 - M_0^{22} and $M_{0.1}^{12}$ - $M_{0.9}^{12}$ respectively. The vertical axis (distance from the oceanic plate) has been corrected for the bending of the plate. The horizontal axis represents the distance of sediments from the trench. The grey colour of the markers indicates that these sediments have been eroded/reworked due to slope failure. The broken black line represents the mean % R_0 attained sediment at a given distance from the trench. λ represents the horizontal periodicity in mean % R_0 for the given model.



530
 531
 532

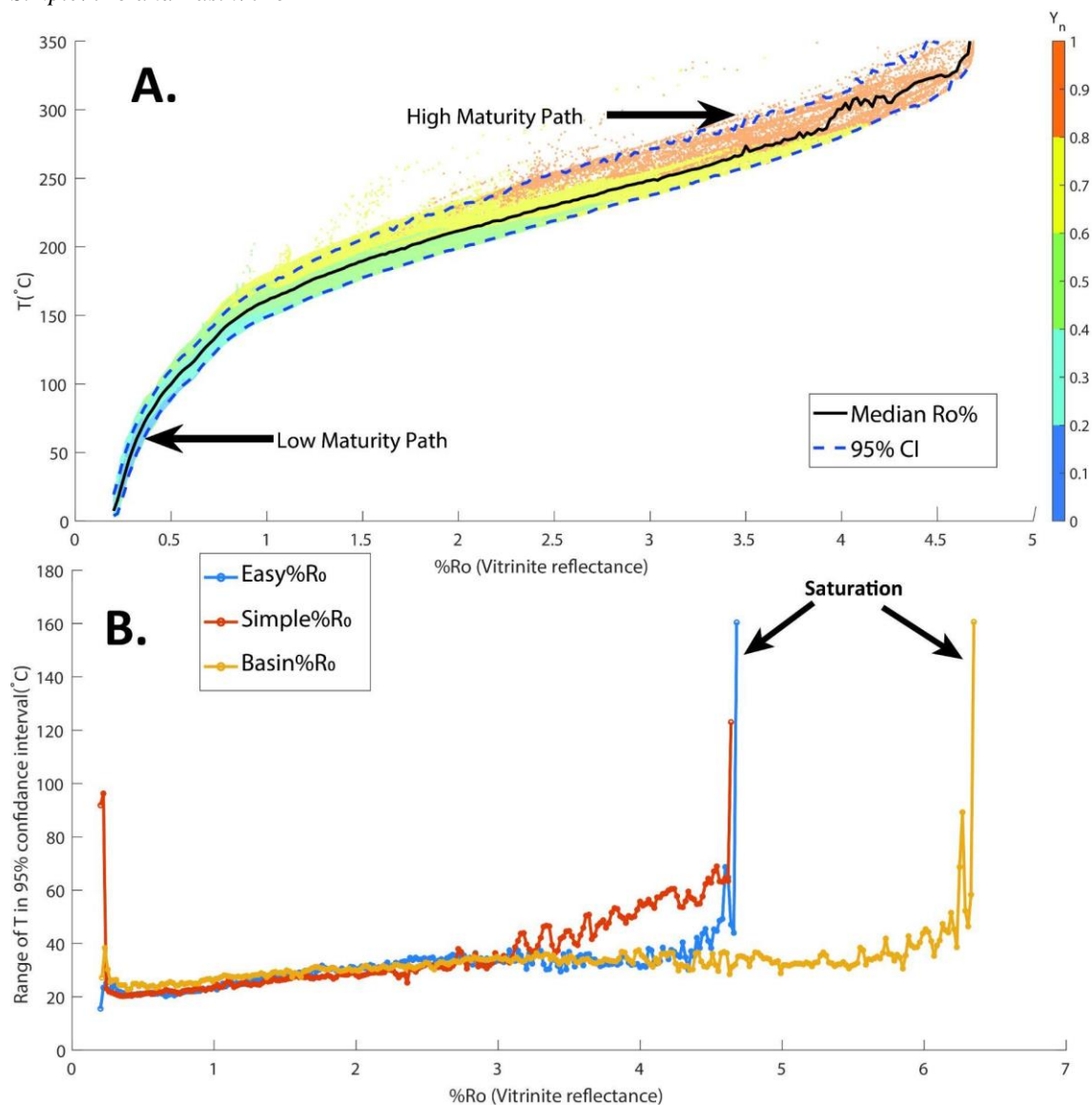


533

534

535

Fig: 4 A. Vitrinite Reflectance ($R_0\%$) vs Maximum Exposure temperature in all models **B.** Range of 95% CI for Easy%Ro, Simple%Ro and Basin%Ro



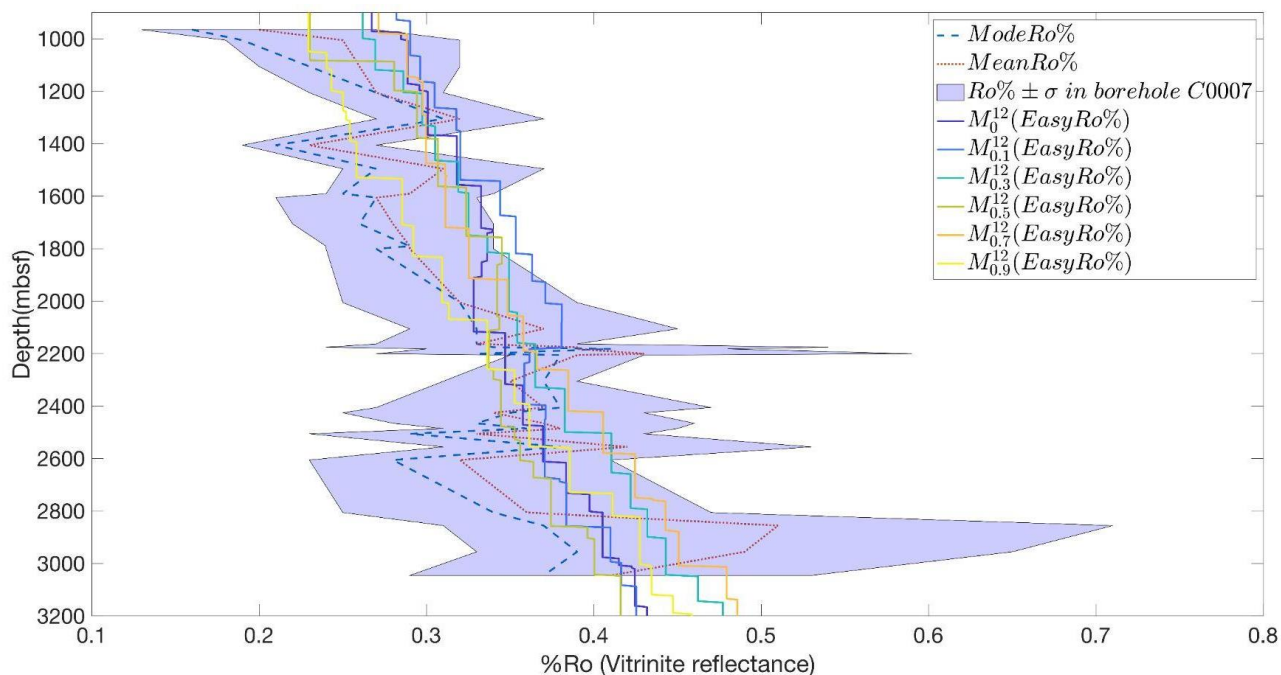
536

537

538



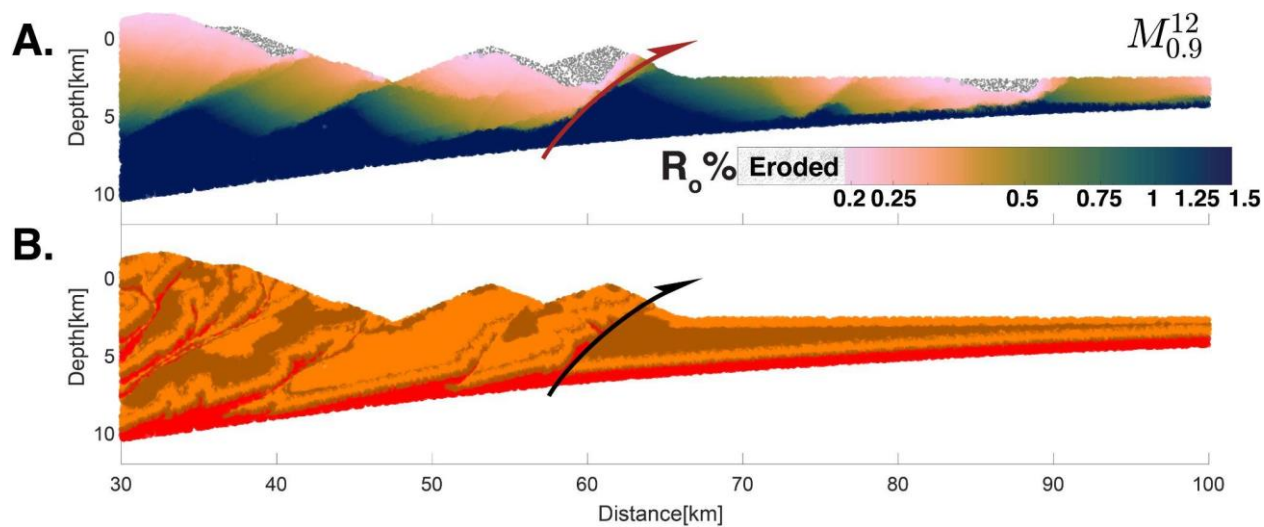
539 **Fig.5:** Depth vs Thermal maturity(% R_o). The shaded (in violet) region shows the range of observed $R_o\%$ ($mean \pm 1SD$) from
540 the C0002 borehole (Fukuchi et al., 2017), colored lines represent the values in models M_0^{12} , $M_{0.1}^{12}$, $M_{0.3}^{12}$, $M_{0.5}^{12}$, $M_{0.7}^{12}$, $M_{0.9}^{12}$.



541
542
543
544
545
546
547
548
549
550
551
552
553
554
555
556
557
558
559
560
561
562
563
564
565



566 **Fig. 6:** Panel A Mapping of eventual thermal maturity(vitrinite reflectance at 7.5Myr) to a frontal thrust at ~4Myr in model
567 $M_{0.9}^{12}$. The lithology of the wedge is shown in panel B. The half arrow represents the active frontal thrust.



568

569

570

571

572

573

574



575 **Fig. 7:** Position dependency of thermal maturity preservation. Panel A. Model state at ~2.5 Myr with a thermal anomaly
576 placed at 110-125 km from backstop B. Model state at ~2.5 Myr with a thermal anomaly placed at 140-155 km from the
577 backstop. C. Model state at ~7.5 Myr.

